https://doi.org/10.1016/j.enconman.2020.113391

Configuration design and parametric optimum selection of a self-supporting PEMFC

Xiuqin Zhang[a], Meng Ni[b], Junyi Wang[a], Lan Yang[a], Xingyu Mao[a], Sunqing Su[a], Zhimin Yang[c,*], Jincan Chen[d]

[a]Department of Physics, Jimei University, Xiamen 361021, People's Republic of China

[b]Department of Building and Real Estate, The Hong Kong Polytechnic University, Hong Kong, People's Republic of China

[c]School of Physics and Electronic Information, Yan'an University, Yan'an 716000, People's Republic of China

[d]Department of Physics, Xiamen University, Xiamen 361005, People's Republic of China

Abstract: A new theoretical model of the thermally self-sustained proton exchange membrane fuel cell (PEMFC) is proposed, where syngas is preheated by the heat from the reaction in the fuel cell and water gas shift reactions, and the endothermic steam reforming process of methane is maintained by absorbing a part of the combustion heat of residuary hydrogen from the fuel cell. Based on some thermal equilibrium equations, the temperatures of syngas and combustion product in different stages are calculated, respectively. The power density and conversion efficiency of the PEMFC are derived. The influences of the molar flow rate of syngas, hydrogen utilization ratio, and working temperature of the fuel cell on the property of the PEMFC are discussed detailedly. In the rational range of the operating temperature, the maximum power densities and corresponding efficiencies are calculated, the optimum values of several key parameters at the maximum power densities are determined, and the optimal selection criteria of molar flow rate of syngas and other parameters are provided.

Keywords: Proton exchange membrane fuel cell; Steam reforming; Self-supporting operation; Maximum power density; Parametric optimum selection

* Email: zhiminyoung@hotmail.com

Nomenclature

A_c Effective surface area, cm^2	V_{con} Concentration overpotential, V
$C_{k,m}$ Molar heat capacity of component k, J $mol^{-1}K^{-1}$	V_{act} Activation overpotential, V
F Faraday constant, C mol^{-1}	V_{ohm} Ohm overpotential, V
$g(T)$ Molar Gibbs function, J mol^{-1}	x Dry gas molar ratio
$h(T)$ Molar enthalpy, J mol^{-1}	x_k Molar fraction of component k
h^0 Molar enthalpy at room temperature, J mol^{-1}	**Greek symbols**
$\dot{H}_1$ Enthalpy of gases leaving SR, J s^{-1}	α Charge transfer coefficient
$\dot{H}_2$ Enthalpy of gases into anode, J s^{-1}	β_1 Parameter in Eq. (14)
$\lvert\Delta\dot{H}\rvert$ Enthalpy change of gases per unit time, J s^{-1}	β_2 Constant
$\dot{H}_{in}$ Enthalpy of gases into burner, J s^{-1}	δ_a Stoichiometry coefficient
$\dot{H}_{out}$ Enthalpy of gases leaving burner, J s^{-1}	δ_c Stoichiometry coefficient
i Current density, A cm^{-2}	δ_{mem} Membrane thickness, cm
I Electric current, A	η Efficiency
i_0 Exchange current density, A cm^{-2}	σ_{mem} Membrane conductivity, $\Omega^{-1}cm^{-1}$
i_L Limiting current density, A cm^{-2}	**Subscripts**
$L_{H_2O,m}$ Latent heat, J mol^{-1}	a Anode
n Mole flow rate, mol s^{-1}	c Cathode
n^* Mole flow rate per unit area, mol $s^{-1}cm^{-2}$	k kth component
n_e Number of electrons	max Maximum
p Pressure, atm	mem Membrane
P Power, J s^{-1}	P State of maximum power density

P^* Power density, J $s^{-1}cm^{-2}$	s Saturation
q_1 Heat flow rate, J s^{-1}	**Abbreviations**
q_1^* Heat flow rate per unit area, J $s^{-1}cm^{-2}$	AB After burner
q_2 Waste heat flow rate, J s^{-1}	HE1 Heat exchanger 1
q_2^* Waste heat flow rate per unit area, J $s^{-1}cm^{-2}$	HE2 Heat exchanger 2
q_k Lower heating value of component k per molar, J mol^{-1}	HTS High-temperature WGS reaction
	LTS Low-temperature WGS reaction
R Universal gas constant, J $mol^{-1}K^{-1}$	PEMFC Proton exchange membrane fuel cell
s^0 Molar entropy at room temperature, J mol^{-1} K^{-1}	PROX Preferential oxidation reaction
$s(T)$ Molar entropy, J mol^{-1} K^{-1}	SR Steam reforming
T Temperature, K	WGS Water gas shift
T_C Combustion temperature, K	
u_{H_2} Hydrogen utilization ratio	

24

1. Introduction

Proton exchange membrane fuel cells (PEMFCs) have the advantages of low pollution, high efficiency, quiet operation, and rapid start, and are promising energy conversion devices. They are potential to power fuel cell vehicles because of their high power density and low operating temperature. However, the relatively poor durability and high cost hinder the application of PEMFCs in fuel cell vehicles [1-3]. To achieve stable operation of a PEMFC, the mechanical behaviors of various sealing materials have been analyzed, a suitable sealing material is chosen to apply to the compression and temperature variation in a fuel cell [4].

In fuel cells, gas starvation is found to be one cause of the lifetime decay [5]. The oxygen starvation will lead to carbon support corrosion and performance degradation [6]. If a carbon nanotube is used as the oxygen reduction reaction catalyst at the cathode, the carbon oxidation could be suppressed [7]. Some researchers pointed out that the metallic bipolar plates have excellent electrical conductivity [8, 9] and corrosion resistance [10]. For the uniform temperature distribution and weight reduction, a new aluminum bipolar plate is suggested to replace the traditional graphite bipolar plate [11]. Because magnesium ion from bipolar plates could be reacted in the PEMFC to form the new sulfonate structure, the effect of Mg^{2+} contamination on the performance degradation is investigated experimentally [12]. A degradation model of membrane and electrodes was designed [13, 14], which will be used to estimate the aging state of a PEMFC.

The uneven distribution of temperature and water in a fuel cell can promote the performance degradation. Temperature instability related to the current change was analyzed experimentally [15, 16]. In fact, the waste heat from current change can be utilized in time to maintain the temperature constant [17]. For even water distribution in the cell, water management was studied experimentally [18-21], a microporous layer is applied to gas diffusion layers [22, 23], and a two-way hydrogen supply mode was applied [24]. Some numerical results [25] showed that if the ionomer volume fraction in catalyst layer is increased, the water flooding in electrodes

may be avoided. The water characteristics in a PEMFC were quantified instantly by considering the cathode liquid water accumulation [26] and anode membrane drying [27].

Improving power density or energy utilization efficiency [28] of a PEMFC can also accelerate the commercialization process. When syngas derived from renewable sources is used in a PEMFC, external reformer for steam reforming (SR) and water gas shift (WGS) reactions is usually needed to convert the syngas into pure hydrogen. By considering the endothermic nature of the reforming reaction and the heat needed for preheating the syngas, the residual hydrogen leaving the anode will be combusted for the SR reaction of hydrocarbon [29]. So the careful thermal management of a PEMFC is critical to achieve high energy conversion efficiency and reliable operation, and the low-grade but large-amount waste heat from a fuel cell is useful [30, 31]. Here, the heats from a PEMFC and WGS reactions is used to preheat the gases, the residual hydrogen is burned to maintain the SR reaction. When some thermal equilibrium equations are satisfied, the maximum power densities of the PEMFC at differently working temperatures are determined and the optimization criteria of some key parameters are provided.

2. Configuration and operating principles

The diagram of a PEMFC is shown schematically in Fig. 1, where abbreviations HE, SR, HTS, LTS, PROX, and AB indicate, respectively, the heat exchanger, steam reforming, high-temperature WGS reaction, low-temperature WGS reaction, preferential oxidation reaction, and after burner. First, syngas flows through the cooling tube of a PEMFC stack to absorb waste heat from the electrochemic reaction, and the temperature of the syngas increases to T_1; Second, the heat released from the HTS, LTS, and PROX is absorbed by the syngas, whose temperature increases to T_2; Third, the syngas is further heated to T_{SR} through the HE1. The heat needed in SR is supplied by the combustion heat of residuary hydrogen of the fuel cell. The gases after the SR

reaction release some heat through the HTS, LTS, and PROX and their temperature decreases to T, which is the operating temperature of the fuel cell. During the electrochemic reaction, the residual gases in the fuel cell flow through the AB, SR, and HE1 then into the environment. T_C, $T_C^{'}$, and $T_C^{''}$ are the temperatures of gases leaving the AB, SR, and HE1, respectively.

2.1. SR and WGS reactions

Syngas is composed of CH_4, CO, H_2, H_2O, CO_2, and N_2. In order to eliminate methane and carbon monoxide [32] in gases, they need to join SR, HTS, LTS, and PROX in turn. Methane and water vapor take part in the SR reaction after preheating, i.e.,

$$CH_4 + H_2O \Leftrightarrow CO + 3H_2 . \quad (1)$$

Carbon monoxide and water vapor participate the HTS and LTS. The temperatures of the HTS and LTS are about 673.15K and 423.15K, respectively, and the chemical reactions are the same, i.e.,

$$CO + H_2O \Leftrightarrow CO_2 + H_2 . \quad (2)$$

There may be residual carbon monoxide in gases after the HTS and LTS, so some extra oxygen needs to be input to eliminate carbon monoxide in the PROX. For easy calculation, the trace oxygen input is neglected and carbon monoxide is assumed to be reacted fully in WGS reactions.

Eq. (1) is endothermic while Eq. (2) is exothermic. If all methane is reacted in Eq. (1), the component of gases after SR reaction can be obtained. The enthalpy of gases is [33]

$$\dot{H}_1 = n[(x_{CH_4} + x_{CO})h_{CO}(T_{SR}) + (3x_{CH_4} + x_{H_2})h_{H_2}(T_{SR}) + (x_{H_2O} - x_{CH_4})h_{H_2O}(T_{SR}) + x_{CO_2}h_{CO_2}(T_{SR}) + x_{N_2}h_{N_2}(T_{SR})], \quad (3)$$

where n is the molar flow rate of syngas, x_k is the molar fraction of component k in syngas, $h_k(T_{SR})$ is the molar enthalpy of k at T_{SR}, i.e.,

$$h_k(T_{SR}) = h_k^0 + \int_{298.15}^{T_{SR}} C_{k,m}\,dt , \quad (4)$$

h_k^0 is the molar enthalpy of k at room temperature (298.15K), $C_{\mathrm{k,m}}$ is the heat capacity per molar of k under constant pressure, and t is the temperature.

The total enthalpy of gases flowing into the anode of a PEMFC is [33]

$$\dot{H}_2 = n[(4x_{\mathrm{CH_4}} + x_{\mathrm{CO}} + x_{\mathrm{H_2}})h_{\mathrm{H_2}}(T) + (x_{\mathrm{H_2O}} - 2x_{\mathrm{CH_4}} - x_{\mathrm{CO}})h_{\mathrm{H_2O}}(T) + (x_{\mathrm{CH_4}} + x_{\mathrm{CO}} + x_{\mathrm{CO_2}})h_{\mathrm{CO_2}}(T) + x_{\mathrm{N_2}}h_{\mathrm{N_2}}(T)]. \quad (5)$$

If the pressures of gases leaving the SR and entering into the PEMFC are the same, the amount of heat released from them per unit time is

$$q_1 = \dot{H}_1 - \dot{H}_2. \quad (6)$$

2.2. Electrochemical reaction in a PEMFC

In Fig. 1, the air enters the cathode through the HE2. The products $\mathrm{H_2O}$ and $\mathrm{N_2}$ in the cathode flow through the HE2 into the environment. The heat released from $\mathrm{H_2O}$ and $\mathrm{N_2}$ is sufficient to preheat the air to temperature T. Thus, it is unnecessary to calculate the heat that the preheating air needs in the following discussion. The gases leaving the PROX enter the anode. The reaction in the fuel cell is

$$\mathrm{H_2} + 0.5\mathrm{O_2} \rightarrow \mathrm{H_2O} + \mathrm{Electricit\,y} + \mathrm{Heat}, \quad (7)$$

where oxygen is from the air at the cathode of the fuel cell.

According to Eq. (7), the amount of total energy produced per unit time is

$$\left|\Delta\dot{H}\right| = n(4x_{\mathrm{CH_4}} + x_{\mathrm{CO}} + x_{\mathrm{H_2}})u_{\mathrm{H_2}}(h_{\mathrm{H_2}}(T) + 0.5h_{\mathrm{O_2}}(T) - h_{\mathrm{H_2O}}(T)), \quad (8)$$

where $u_{\mathrm{H_2}}$ is the hydrogen utilization ratio in the electrochemical reaction. The power output is given by

$$P = n(4x_{\mathrm{CH_4}} + x_{\mathrm{CO}} + x_{\mathrm{H_2}})u_{\mathrm{H_2}}(g_{\mathrm{H_2}}(T) + 0.5g_{\mathrm{O_2}}(T) - g_{\mathrm{H_2O}}(T)) - I(V_{act} + V_{ohm} + V_{con}), \quad (9)$$

where

$$g_k(T) = h_k(T) - Ts_k(T) \quad (10)$$

is the molar Gibbs function of component k,

$$s_k(T) = s_k^0 + \int_{298.15}^{T} \frac{C_{k,m}}{t} dt - R \ln p_k \quad (11)$$

is the molar entropy of k, s_k^0 is the molar entropy of k at room temperature, and p_k is the partial pressure. V_{act}, V_{ohm}, and V_{con} are, respectively, activation, ohm, and concentration overpotentials, and I is the electric current. Three overpotentials may be, respectively, expressed as [34]

$$V_{act} = \frac{RT}{n_e F} \frac{(\alpha_a + \alpha_c)}{\alpha_a \alpha_c} \ln \frac{i}{i_0}, \quad (12)$$

$$V_{ohm} = i \frac{\delta_{mem}}{\sigma_{mem}}, \quad (13)$$

and

$$V_{con} = i(\beta_1 \frac{i}{i_L})^{\beta_2}, \quad (14)$$

where n_e is the number of electrons, R is the universal gas constant, F is Faraday's constant, $i = I / A_c$ is the current density, A_c is the effective surface area of bipolar plates, i_0 is the exchange current density, i_L is the limiting current density, α_a and α_c are, respectively, the anode and cathode charge transfer coefficients, δ_{mem} is the thickness of membrane, σ_{mem} is the conductivity of membrane, β_1 depends on T and p_{O_2}, and β_2 is constant.

According to the law of energy conservation, when the heat leakage losses from the fuel cell into the environment is ignored, the heat flow rate from the fuel cell to the cooling tube is

$$q_2 = \left|\Delta \dot{H}\right| - P$$

$$= n(4x_{CH_4} + x_{CO} + x_{H_2}) u_{H_2} T(s_{H_2}(T) + 0.5 s_{O_2}(T) - s_{H_2O}(T)) + I(V_{act} + V_{ohm} + V_{con}). \quad (15)$$

Based on Faraday's law, the relation between the electric current and the molar flow rate of syngas is

$$I = n(4x_{CH_4} + x_{CO} + x_{H_2}) u_{H_2} n_e F. \quad (16)$$

By combining Eqs. (3) - (6) and (10) - (16) with Tables (1) - (3) [17, 35-39], the curves of $q_1^* = q_1 / A_c$ and $q_2^* = q_2 / A_c$ varying with $n^* = n / A_c$ are shown in Fig. 2, where T_{SR} =873.15K and T =353.15K. q_1^* is irrelevant to u_{H_2}, while q_2^* is a monotonically increasing function of u_{H_2}. The values of some parameters in

Fig. 2 are used in the following figures. According to Eqs. (9) - (14) and (16), we can plot the three-dimensional graph of the power density $P^* = P / A_C$ [40] varying with n^* and u_{H_2}, as indicated in Fig. 3. Fig. 3 presents that the power density is not a monotonic function of n^* and u_{H_2}. When n^* =3.85×10^{-5} (mol s^{-1}cm^{-2}) and u_{H_2} =0.677, the power density attains its maximum, 0.66 (J s^{-1}cm^{-2}).

3. The preheating of syngas by means of q_1 and q_2

It can be found from Eq. (15) and Tables (1) - (3) that

$$q_2 \geq n\sum_k (x_k \int_{298.15}^{T_1} C_{k,m} dt) . \quad (17)$$

It can be also found that even if T_1 is equal to T, Eq. (17) is still satisfied. Usually, T_1 is lower than T so that the heat exchange process can be finished in the given finite time. In the following discussion, $T_1 = T - 5$ is assumed.

When the heat q_1 is absorbed by syngas, whose temperature rises from T_1 to T_2, one obtains

$$q_1 = n\sum_k (x_k \int_{T_1}^{T_2} C_{k,m} dt). \quad (18)$$

It can be found from Eqs. (3), (5), (6), and (18) that T_2 is independent of n, but it is a function of T_1, T, and T_{SR}. T_2 is still lower than T_{SR}. Syngas through the HE1 is heated to T_{SR} and absorbs the heat in the SR reaction. The heats what syngas needs in such two processes comes from the combustion of residual hydrogen, which will be further discussed in next section.

4. The SR and preheating of syngas by means of combustion

It is assumed that the air entering a burner is just used up. The total enthalpy of gases flowing into the burner is

$$\dot{H}_{in} = n[(4x_{CH_4} + x_{CO} + x_{H_2})(1-u_{H_2})h_{H_2}(T) + (x_{H_2O} - 2x_{CH_4} - x_{CO})h_{H_2O}(T) + (x_{CH_4} + x_{CO} + x_{CO_2})h_{CO_2}(T) +$$

$$x_{N_2} h_{N_2}(T)] + 0.5n(4x_{CH_4} + x_{CO} + x_{H_2})(1-u_{H_2})[h_{O_2}(T_O) + 3.762h_{N_2}(T_O)]. \quad (19)$$

The component of combustion product is determined according to combustion reactions and the enthalpy is

$$\dot{H}_{out} = n[2x_{CH_4} + x_{H_2O} + x_{H_2} - (4x_{CH_4} + x_{H_2} + x_{CO})u_{H_2}]h_{H_2O}(T_C) + n(x_{CH_4} + x_{CO} + x_{CO_2})h_{CO_2}(T_C) +$$

$$n[1.881(4x_{CH_4} + x_{CO} + x_{H_2})(1-u_{H_2}) + x_{N_2}]h_{N_2}(T_C). \quad (20)$$

If there is no heat leakage in the burner,

$$\dot{H}_{in} = \dot{H}_{out}. \quad (21)$$

It is seen from Eqs. (19) - (21) that T_C is a function of u_{H_2} and T. If the high-temperature heat in combustion product is absorbed by syngas in SR reaction and preheating, one can obtain the following relations

$$x_{CH_4}(h_{CO}(T_{SR}) + 3h_{H_2}(T_{SR}) - h_{CH_4}(T_{SR}) - h_{H_2O}(T_{SR})) = (x_{CH_4} + x_{CO} + x_{CO_2})\int_{T_C'}^{T_C} C_{CO_2,m}dt +$$

$$[2x_{CH_4} + x_{H_2O} + x_{H_2} - (4x_{CH_4} + x_{H_2} + x_{CO})u_{H_2}]\int_{T_C'}^{T_C} C_{H_2O,m}dt + [1.881(4x_{CH_4} + x_{CO} + x_{H_2})(1-u_{H_2}) + x_{N_2}]\int_{T_C'}^{T_C} C_{N_2,m}dt \quad (22)$$

and

$$\sum_k (x_k \int_{T_2}^{T_{SR}} C_{k,m}dt) = [2x_{CH_4} + x_{H_2O} + x_{H_2} - (4x_{CH_4} + x_{H_2} + x_{CO})u_{H_2}]\int_{T_C''}^{T_C'} C_{H_2O,m}dt +$$

$$(x_{CH_4} + x_{CO} + x_{CO_2})\int_{T_C''}^{T_C'} C_{CO_2,m}dt + [1.881(4x_{CH_4} + x_{CO} + x_{H_2})(1-u_{H_2}) + x_{N_2}]\int_{T_C''}^{T_C'} C_{N_2,m}dt. \quad (23)$$

By using Eqs. (18) - (23), the curves of T_C, T_C', T_C'', and T_2 varying with T under a given T_{SR} are illustrated in Fig. 4. It is clearly obtained from Fig. 4 that

$$T_C' > T_{SR} \quad (24)$$

and

$$T_C'' > T_2. \quad (25)$$

According to Eqs. (22) - (25), if a self-supporting SR reaction and preheating of syngas are both guaranteed, the maximum hydrogen utilization ratio is 0.75 when 340.15<T<368.15K and T_{SR}=873.15K. When T_{SR} increases to 1023.15K, the maximum available hydrogen utilization ratio will decrease to 0.66.

5. The efficiency of a PEMFC

The components CH_4, CO, and H_2 in syngas are combustible, so the efficiency of the system is

$$\eta = \frac{P}{n(x_{CH_4} q_{CH_4} + x_{CO} q_{CO} + x_{H_2} q_{H_2})}$$

$$= \frac{(4x_{CH_4} + x_{CO} + x_{H_2}) u_{H_2} [g_{H_2}(T) + 0.5 g_{O_2}(T) - g_{H_2O}(T) - n_e F(V_{act} + V_{ohm} + V_{con})]}{x_{CH_4} q_{CH_4} + x_{CO} q_{CO} + x_{H_2} q_{H_2}}, \quad (26)$$

where q_k is the lower heating value of component *k*. According to (26), Fig. 5 gives the three-dimensional graph of the efficiency η varying with n^* and u_{H_2} and shows that η is a monotonically decreasing function of n^* but a monotonic function of u_{H_2}. The curve shape of η varying with u_{H_2} is the same as that of P^* varying with u_{H_2} because the difference between η and P^* is only a proportional constant for the given values of n^*.

6. Results and discussion

In order to obtain both the power density and the efficiency as large as possible, it is necessary to reasonably select both n^* and u_{H_2}. From Figs. 3 and 5, we can determine that the optimum range of n^* is

$$n^* \le n_P^* \quad (27)$$

and the optimum value of u_{H_2} is

$$u_{H_2} = u_{H_2,P}, \quad (28)$$

where n_P^* and $u_{H_2,P}$ are the corresponding values of n^* and u_{H_2} at the maximum power density P_{max}^*, respectively. It can be proved from Eqs. (9) and (26) that using extremum conditions $\partial P^* / \partial u_{H_2} = 0$ and $\partial \eta / \partial u_{H_2} = 0$, one can get Eq. (28).

Using Eqs. (9), (26), and (28), one can further generate the power density versus the efficiency curve, as illustrated in Fig. 6, where η_P is the efficiency at P_{max}^*. It can be observed from Fig. 6 that when $\eta < \eta_P$,

200 P^* increases with the increase of η. Thus, the efficiency should be in the range of

201 $$\eta \geq \eta_P . \quad (29)$$

202 In such a range, P^* decreases with the increase of η, and consequently, both the efficiency and the power

203 density should be considered at the same time.

204 The curves in Fig. 6 also indicate that both $P^*_{\max}$ and η_P are monotonically decreasing functions of the

205 working temperature of a PEMFC. In the range of 340.15~368.15 K, the curves of $P^*_{\max}$ and η_P varying with

206 T are illustrated in Fig. 7(a), which shows that the lower the temperature of a PEMFC is, the larger the

207 maximum power density and corresponding efficiency. Thus, one should try to keep the working temperature T

208 as low as possible in the operation of a PEMFC. Fig.7(b) further shows the curves of n^*_P and $u_{\mathrm{H}_2,P}$ varying

209 with T. Although n^*_P and $u_{\mathrm{H}_2,P}$ are not monotonic functions of T in the range of 340.15~368.15 K, the

210 variation ranges of n^*_P and $u_{\mathrm{H}_2,P}$ are very small and less than 3×10^{-7} (mol $s^{-1}cm^{-2}$) and 0.005, respectively.

211 According to Eqs. (27) and (28) and Fig.7(b), one can reasonably select the values of n^* and u_{H_2} so that the

212 PEMFC is operated in the optimal states.

213

214 **7. Conclusions**

215 A self-supporting model of the PEMFC based on syngas has been established. The waste heat from the

216 electrochemical and WGS reactions is utilized for the preheating of fuel and a part of the combustion heat of

217 residual fuel is used in the process of the SR reaction so that no additional external heat input is required. The

218 whole performance of the PEMFC is evaluated and key parameters are optimized. In the range of

219 340.15~368.15K, the maximum power density and corresponding efficiency are monotonically decreasing

220 functions of the working temperature of the fuel cell, while the hydrogen utilization ratio and molar flow rate of

221 syngas at the maximum power density have only slight changes and may be approximated as constant. The

PEMFC should be controlled to be operated at low temperatures. For example, at the working temperature of 340.15 K, the maximum power density and the efficiency, hydrogen utilization ratio, and molar flow rate of syngas at the maximum power density can attain 0.67 (J $s^{-1}cm^{-2}$), 0.207, 0.674, and 3.83×10^{-5} (mol $s^{-1}cm^{-2}$), respectively. These results may provide some theoretical guidance for the optimal design and best operation of practical PEMFCs.

Acknowledgements

This work was supported by Youth Top Talent Program (No. ZR2018001) of Jimei University, Distinguished Young Scholars (No. B17164) of Fujian Province, and National Natural Science Foundation (No. 11605073), People's Republic of China.

References

[1] Vichard L, Petrone R, Harel F, Ravey A, Venet P, Hissel D. Long term durability test of open-cathode fuel cell system under actual operating conditions. Energy Convers Manage 2020; 212: 112813.

[2] Paul M, Saha M, Qi W, Stumper J, Gates B. Microstructured membranes for improving transport resistances in proton exchange membrane fuel cells. Int J Hydrogen Energy 2020; 45: 1304-12.

[3] Tang Z, Huang Q, Wang Y, Zhang F, Li W, Li A, Zhang L, Zhang J. Recent progress in the use of electrochemical impedance spectroscopy for the measurement, monitoring, diagnosis and optimization of proton exchange membrane fuel cell performance. J Power Sources 2020; 468: 228361.

[4] Qiu D, Liang P, Peng L, Yi P, Lai P, Ni J. Material behavior of rubber sealing for proton exchange membrane fuel cells. Int J Hydrogen Energy 2020; 45: 5465-73.

[5] Chen H, Zhao X, Zhang T, Pei P. The reactant starvation of the proton exchange membrane fuel cells for vehicular applications: A review. Energy Convers Manage 2019; 182: 282-98.

[6] Meyer Q, Pivac I, Barbir F, Zhao C. Detection of oxygen starvation during carbon corrosion in proton exchange membrane fuel cells using low-frequency electrochemical impedance spectroscopy. J Power Sources 2020; 470: 228285.

[7] Cha B, Jun S, Jeong B, Ezazi M, Kwon G, Kim D, Lee D. Carbon nanotubes as durable catalyst supports for oxygen reduction electrode of proton exchange membrane fuel cells. J Power Sources 2018; 401: 296-302.

[8] Qiu D, Peng L, Yi P, Lai X, Lehnert W. Flow channel design for metallic bipolar plates in proton exchange membrane fuel cells: Experiments. Energy Convers Manage 2018; 174: 814-23.

[9] Li S, Zhou W, Liu R, Huang J, Chu X. Fabrication of porous metal fiber sintered sheet as a flow field for proton exchange membrane fuel cell. Current Appl Physics 2020; 20: 686-95.

[10] Song Y, Zhang C, Ling C, Han M, Yong R, Sun D, Chen J. Review on current research of materials,

fabrication and application for bipolar plate in proton exchange membrane fuel cell. Available at: https://doi.org/10.1016/j.ijhydene.2019.07.231.

[11] Awin Y, Dukhan N. Experimental performance assessment of metal-form flow fields for proton exchange membrane fuel cells. Appl Energy 2019; 252: 1-8.

[12] Zhu J, Tan J, Pan Q, Liu Z, Hou Q. Effects of Mg^{2+} contamination on the performance of proton exchange membrane fuel cell. Energy 2019; 189: 1-11.

[13] Liu H, Chen J, Hissel D, Hou M, Shao Z. A multi-scale hybrid degradation index for proton exchange membrane fuel cells. J Power Sources 2019; 437: 1-13.

[14] Ren P, Pei P, Li Y, Wu Z, Chen D, Huang S. Degradation mechanisms of proton exchange membrane fuel cell under typical automotive operating conditions. Progress in Energy and Combustion Science 2020; 80: 100859.

[15] Luo L, Jian Q, Huang B, Huang Z, Zhao J, Cao S. Experimental study on temperature characteristics of an air-cooled proton exchange membrane fuel cell stack. Renew Energy 2019; 143: 1067-78.

[16] Zhao J, Huang Z, Jian B, Bai X, Jian Q. Thermal performance enhancement of air-cooled proton exchange membrane fuel cells by vapor chambers. Energy Convers Manage 2020; 213: 112830.

[17] Zhang X, Lin Q, Liu H, Chen X, Su S, Ni M. Performance analysis of a proton exchange membrane fuel cell based syngas. Entropy 2019; 21(1): 1-12.

[18] Simari C, Lufrano E, Brunetti A, Barbieri G, Nicotera I. Highly-performing and low-cost nanostructured membranes based on Polysulfone and layered doubled hydroxide for high-temperature proton exchange membrane fuel cells. J Power Sources 2020; 471: 228440.

[19] Guo H, Guo Q, Ye F, Ma C, Zhu X, Liao Q. Three-dimensional two-phase simulation of a unitized regenerative fuel cell during mode switching from electrolytic cell to fuel cell. Energy Convers Manage 2019;

195: 989-1003.

[20] Park H. Effect of the hydrophilic and hydrophobic characteristics of the gas diffusion medium on polymer electrolyte fuel cell performance under non-humidification condition. Energy Convers Manage 2014; 81: 220-30.

[21] Shabani M, Younesi H, Pontié M, Rahimpour A, Rahimnejad M, Zinatizadeh A. A critical review on recent proton exchange membranes applied in microbial fuel cells for renewable energy recovery. J Cleaner Production 2020; 264: 121446.

[22] Ito H, Heo Y, Ishida M, Nakano A, Someya S, Munakata T. Application of a self-supporting microporous layer to gas diffusion layers of proton exchange membrane fuel cells. J Power Sources 2017; 342: 393-404.

[23] Chen L, Lin R, Tang S, Zhong D, Hao Z. Structural design of gas diffusion layer for proton exchange membrane fuel cell at varying humidification. J Power Sources 2020; 467: 228355.

[24] Zhao J, Jian Q, Huang Z, Luo L, Huang B. Experimental study on water management improvement of proton exchange membrane fuel cells with dead-ended anode by periodically supplying fuel from anode outlet. J Power Sources 2019; 435: 226775.

[25] He P, Chen L, Mu Y, Tao W. Modeling of the effect of ionomer volume fraction on water management for proton exchange membrane fuel cell. Energy Procedia 2019; 158: 2139-44.

[26] Xia Z, Wang B, Yang Z, Wu K, Du Q, Jiao K. Effect of operating conditions on performance of proton exchange membrane fuel cell with anode recirculation. Energy Procedia 2019; 158: 1829-34.

[27] Wang R, Zhang G, Hou Z, Wang K, Zhao Y, Jiao K. Comfort index evaluating the water and thermal characteristics of proton exchange membrane fuel cell. Energy Convers Manage 2019; 185: 496-507.

[28] Lü X, Wu Y, Lian J, Zhang Y, Chen C, Wang P, Meng L. Energy management of hybrid electric vehicles: A review of energy optimization of fuel cell hybrid power system based on genetic algorithm. Energy Convers

Manage 2020; 205: 112474.

[29] Zhang S, Zhang Y, Chen J, Yin C, Liu X. Design, fabrication and performance evaluation of an integrated reformed methanol fuel cell for portable use. J Power Sources 2018; 389: 37-49.

[30] Jo A, Oh K, Lee J, Han D, Kim D, Kim J, et al. Modeling and analysis of a 5 kW_e HT-PEMFC system for residential heat and power generation. Int J Hydrogen Energy 2017; 42: 1698-714.

[31] Nguyen H, Shabani B. Proton exchange membrane fuel cells heat recovery opportunities for combined heating/cooling and power applications. Energy Convers Manage 2020; 204: 112328.

[32] Yan W, Cheng G, Chen C, Yang T, Ghalambaz M. Effects of reformate on performance of PBI/H_3PO_4 proton exchange membrane fuel cell stack. Int J Hydrogen Energy 2020; 45: 15346-57.

[33] Authayanun S, Mamlouk M, Scott K, Arpornwichanop A. Comparison of high-temperature and low-temperature polymer electrolyte membrane fuel cell systems with glycerol reforming process for stationary applications. Appl Energy 2013; 109: 192-201.

[34] Mert S, Dincer I, Ozcelik Z. Exergoeconomic analysis of a vehicular PEM fuel cell system. J Power Sources 2007; 165: 244-52.

[35] Rowe A, Li X. Mathematical modeling of proton exchange membrane fuel cells. J Power Sources 2001; 102: 82-96.

[36] Shin Y, Park W, Chang J, Park J. Evaluation of the high temperature electrolysis of steam to produce hydrogen. Int J Hydrogen Energy 2007; 32: 1486-91.

[37] Zhang Y, Mawardi A, Pitchumani R. Numerical studies on an air-breathing proton exchange membrane (PEM) fuel cell stack. J Power Sources 2007; 173: 264-76.

[38] Ay M, Midilli A, Dincer I. Exergetic performance analysis of a PEM fuel cell. Int J Energy Res 2006; 30: 307-21.

321 [39] Zhang X, Ni M, He W, Dong F. Theoretical analysis and optimum integration strategy of the PEM fuel cell
322 and internal combustion engine hybrid system for vehicle applications. Int J Energy Research 2015; 39: 1664-72.
323 [40] Guo Y, Guo X, Zhang H, Hou S. Energetic, exergetic and ecological analyses of a high-temperature proton
324 exchange membrane fuel cell based on a phosphoric-acid-doped polybenzimidazole membrane. Sustainable
325 Energy Technologies and Assessments 2020; 38: 100671.

Table captions:

Table 1. The composition of syngas [17].

Table 2. Thermodynamic parameters of chemical components [17, 35], where (g) and (l) refer to gas and liquid phases, respectively.

Table 3. Parameters used in a PEMFC [34-39].

332 Table 1

Component k	H_2	CH_4	CO	CO_2	H_2O	N_2
Mole fraction x_k	0.13	0.01	0.16	0.05	0.36	0.29

333

334 Table 2

Component k	h_k^0 (J mol^{-1})	s_k^0 (J mol^{-1} K^{-1})	$L_{H_2O,m}$ (J mol^{-1})	Molar heat capacity $C_{k,m}$ (J mol^{-1} K^{-1})
N_2	0	—	—	29.12
O_2	0	205.138	—	$25.8911+0.0129874t-0.0000038644t^2$
CH_4	-75000	—	—	$14.1555+0.0755466t-0.0000180032t^2$
CO_2	-393800	—	—	$26.0167+0.0435259t-0.0000148422t^2$
CO	-110500	—	—	$26.8742+0.006971t-0.0000008206t^2$
H_2	0	130.695	—	$29.0856-0.0008373t+0.0000020138t^2$
H_2O (g)	-241800	—	—	$30+0.01071t+33000/t^2$
H_2O (l)	-285800	69.940	40700	75.44

335

336 Table 3

Parameter and its symbol	Value
Number of electrons: n_e	2
Faraday constant: F (C mol^{-1})	96485
Universal gas constant: R (J mol^{-1} K^{-1})	8.314
Partial pressure of hydrogen: p_{H_2} (atm)	$p_a(1-\frac{p_s}{p_a})/[1+\frac{x_a}{2}(1+\frac{\delta_a}{\delta_a-1})]$ [34]
Partial pressure of oxygen: p_{O_2} (atm)	$p_c(1-\frac{p_s}{p_c})/[1+\frac{x_c}{2}(1+\frac{\delta_c}{\delta_c-1})]$ [34]
Pressure at anode: p_a (atm)	5
Pressure at cathode: p_c (atm)	5
Saturation pressure of water: p_s (atm)	$10^{-2.1794+0.02953(T-273.15)-9.1837\times10^{-5}(T-273.15)^2}$ $\times10^{1.4454\times10^{-7}(T-273.15)^3}$ [35]
Dry gas molar ratio at anode: x_a	$(x_{N_2}+x_{CO_2}+x_{CH_4}+x_{CO})/(x_{H_2}+x_{CO}+4x_{CH_4})$
Dry gas molar ratio at cathode: x_c	3.762 (air)
Stoichiometry coefficients: δ_a and δ_c	1.5 and 3 [36]
Charge transfer coefficient at the anode: α_a	1
Charge transfer coefficient at the cathode: α_c	1
Exchange current density: i_0 (A cm^{-2})	$1.27\times10^{-8}\exp(2.06p_{O_2})$ [37]
Membrane thickness: δ_{mem} (cm)	1.6×10^{-2}
σ_{mem} (Ω^{-1}cm^{-1})	$(0.005139\mu_{mem}-0.003260)\exp[1268(\frac{1}{303}-\frac{1}{T})]$ [36]
μ_{mem}	14 [36]
β_1	$(8.66\times10^{-5}T-0.068)(p_{O_2}/0.1173+p_s)$

	$-1.6\times10^{-4}T+0.54$ [38]
Constant: β_2	2 [39]
Limiting current density: i_L (A cm^{-2})	2 [39]
q_k (J mol^{-1}): k=H_2; CO; CH_4	241900; 283200; 803700

337

Figure captions:

Fig. 1. The schematic diagram of a PEMFC.

Fig. 2. The curves of q_1^* and q_2^* varying with n^*.

Fig. 3. The three-dimensional graph of the power density P^* varying with n^* and u_{H_2}.

Fig. 4. The curves of T_C, $T_C^{'}$, $T_C^{''}$, and T_2 varying with T, respectively, where u_{H_2} =0.75.

Fig. 5. The three-dimensional graph of the efficiency η varying with n* and u_{H_2}.

Fig. 6. The curves of the power density P^* varying with efficiency η for the given values of T and $u_{\mathrm{H}_2} = u_{\mathrm{H}_2,P}$.

Fig. 7. The curves of (a) $P_{\max}^*$ and η_P and (b) n_P^* and $u_{\mathrm{H}_2,P}$ varying with T.

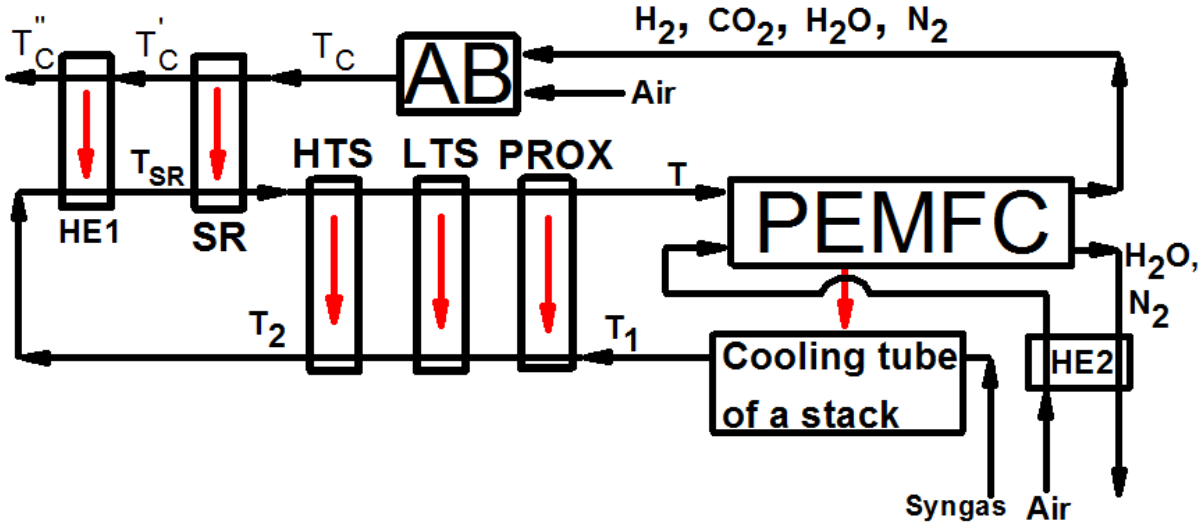

348

349 Fig. 1

350

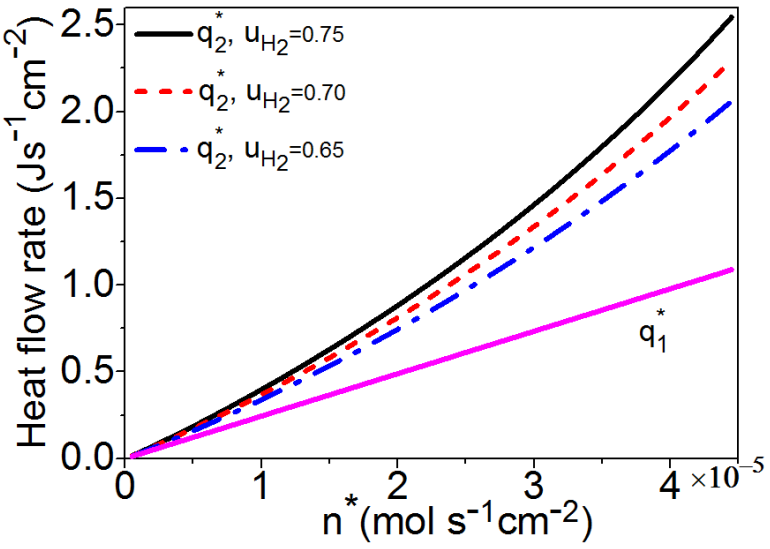

351

352 Fig. 2

353

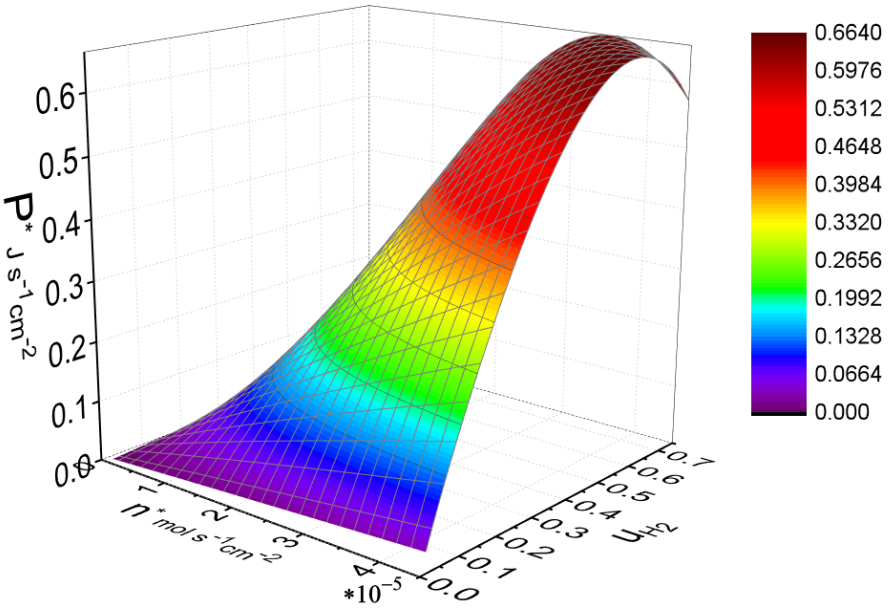

354

355 Fig. 3.

356

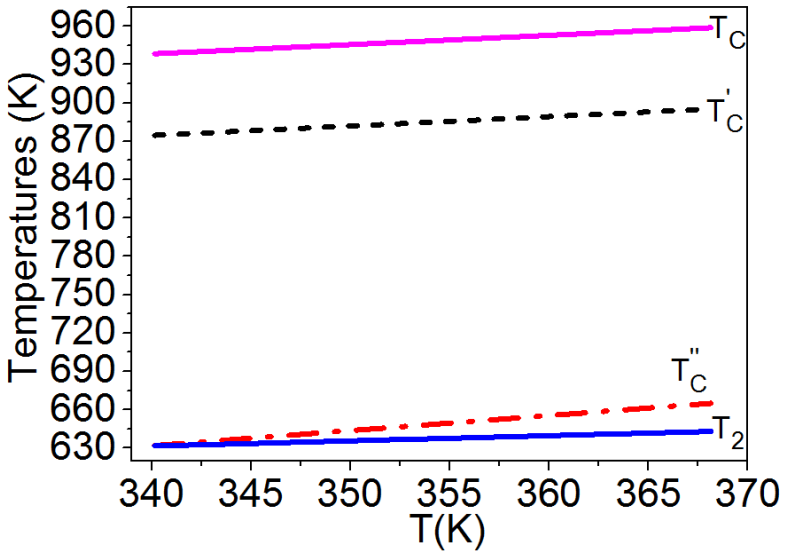

357

358 Fig. 4.

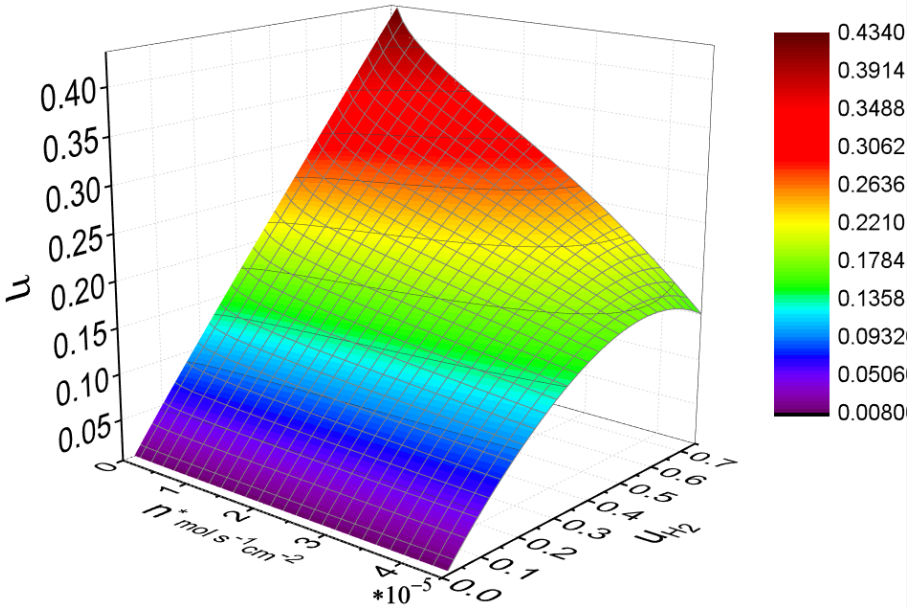

359

360 Fig. 5.

361

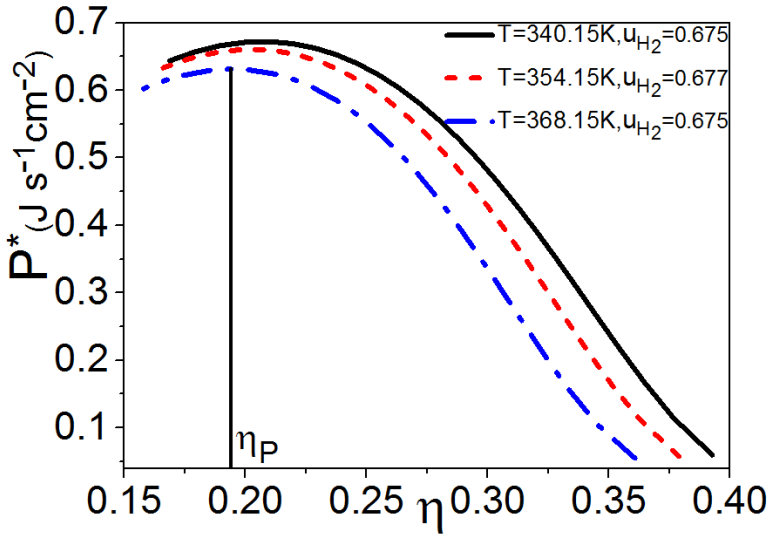

362

363 Fig. 6.

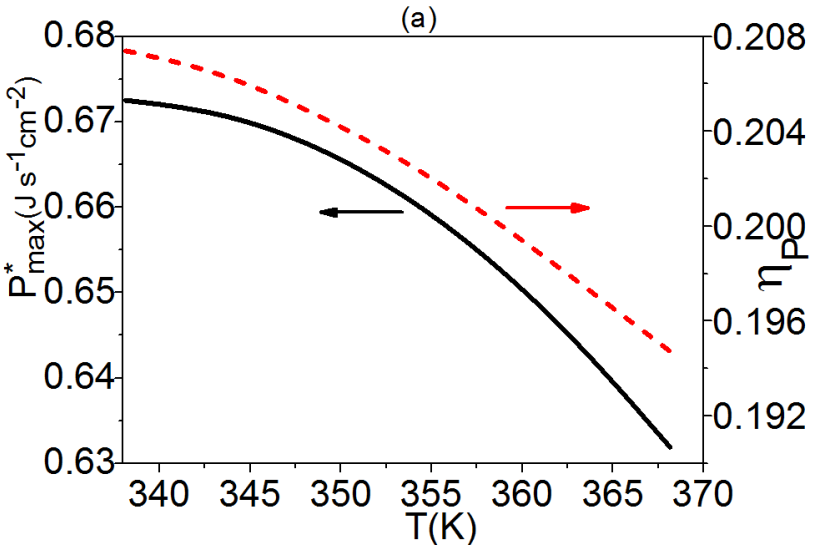

364

365

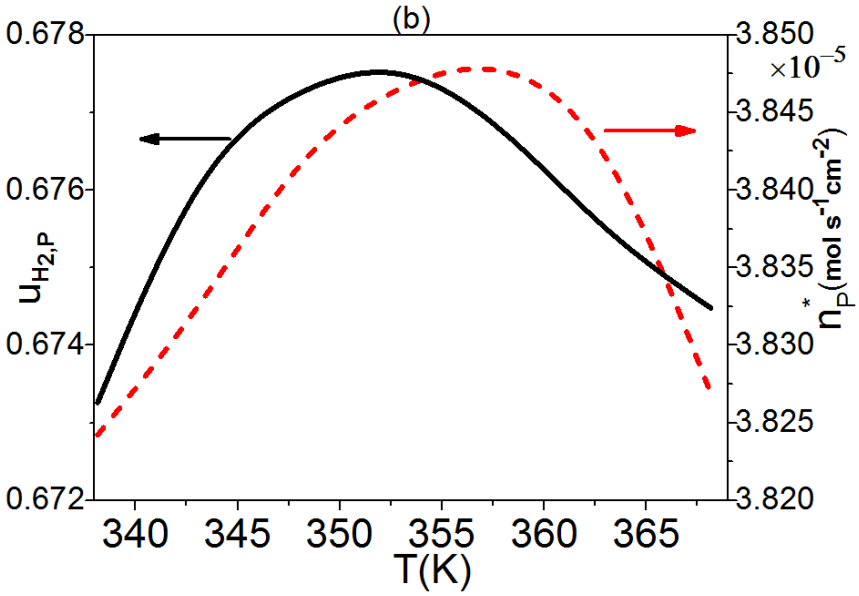

366

367 Fig. 7.